AIAA JOURNAL
Vol. 39, No. 6, June 2001

Numerical Simulation of Wake Vortex Detection Using a Radio Acoustic Sounding System

Said Boluriaan* and Philip J. Morris†
Pennsylvania State University, University Park, Pennsylvania 16802

A parallel, two-dimensional Euler, one-dimensional Maxwell code is developed to numerically simulate wake vortex detection using a radio acoustic sounding system. The code is written in Fortran 90 with the message passing interface for parallel implementation. The main difficulty with a time-accurate simulation is the number of samples required to resolve the Doppler shift in the scattered electromagnetic signal. Even for a one-dimensional simulation with typical scatterer size, the CPU time required to run the code is far beyond currently available computer resources. Two alternatives that overcome this problem are described. In the first, the code is run for a fictitious speed of light. Second, the governing differential equations are recast in order to remove the carrier frequency and solve only for the frequency shift using an implicit scheme with large time steps. The numerical stability characteristics of the resulting discretized equation with complex coefficients are shown. The code is run for both the approaches with Taylor and Oseen vortex velocity profiles. Finally, the Abel transform is applied to the outputs of both explicit and implicit schemes, and the wake vortex velocity field is retrieved with very good accuracy.

I. Introduction

ALL aircraft generate trailing wake vortices. The production of these vortices is a consequence of the generation of lift. The vortex generated by a large aircraft can have a catastrophic effect on a small plane following closely behind. The National Transportation Safety Board, which is charged with investigating aviation accidents and incidents, has reported that at least 51 wake vortex accidents and incidents in the United States occurred between 1983 and 1993 (Ref. 1).

To ensure protection against wake vortex encounters, the Federal Aviation Administration has imposed a large separation distance behind heavy aircraft during takeoff and landing operations. The wake vortex separation standard is currently determined assuming the worst wake vortex scenario and is considered to be very conservative. For instance, it does not allow for the fact that crosswinds can move wake vortices rapidly out of the glide slope. A wake vortex detection system would increase airport productivity by measuring the wake vortex strength in real time and allowing for an adaptive spacing system to be employed.

A radio acoustic sounding system (RASS) is a remote sensing technique that has been used to measure atmospheric temperature and wind aloft. The concept of a RASS has been applied over the past two decades to the measurement of atmospheric parameters such as temperature, wind velocity, and the turbulence field.[2] Recently, RASS has received particular attention as a potential tool to detect vortices behind aircraft in the vicinity of airports.[3] The basic concept is based on the tracking of sound waves with radar. When acoustic waves with a frequency f_a are transmitted, they propagate at the speed of sound c_a, producing periodic fluctuations in the air permittivity profile with a scale of an acoustic wavelength, $\lambda_a = c_a/f_a$. A radar installed as part of the RASS with an electromagnetic wavelength λ_e illuminates the acoustic waves and receives an echo scattered by the permittivity fluctuations. However, the changes are so slight that no significant return signal would be sensed unless the Bragg condition between the wavelength of the refractive index fluctuations and the radar wavelength is satisfied. The Bragg condition requires that the wavelength of the acoustic wave λ_a be half that of the electromagnetic wave λ_e, i.e., $\lambda_a = \lambda_e/2$.

The spectrum of the scattered field shows a Doppler shift proportional to the local speed of sound. In the presence of an aircraft wake vortex, the effective speed of acoustic propagation will change:

$$c_a = c_{a0} + V_y \tag{1}$$

where c_{a0} is the speed of sound at standard atmospheric conditions and V_y is the local vortex velocity component in the transmitter direction for a monostatic RASS configuration, where the acoustic source and electromagnetic transmitter and receiver are collocated. Therefore, the scattered field spectrum contains information about the vortex velocity profile. The main objective of the present study is to reveal this information from the scattered field spectrum.

To date, the use of a RASS has focused on temperature and wind velocity measurements. Most of the research in this area has been experimental. Although there are a few wake vortex velocity measurements using RASS, there have been no numerical simulations of this application. The numerical simulation of a RASS permits a detailed assessment of the ability of the system to measure the properties of wake vortices including their strength (circulation), location, radial extent, and maximum azimuthal velocity. In addition, the sensitivity of the measurement system to changes in operating parameters, environmental conditions, and distortions of the wake vortex may also be assessed.

In almost all RASS analyses the permittivity perturbation has been modeled by a periodic or simple stochastic function to describe the fluctuations of temperature, wind velocity, heat flux, and the effect of turbulence. No one has performed a direct computation of permittivity fluctuations based on the first principle equations. This is mainly because a direct computation of the acoustic field had not been feasible, considering the enormous difference between the acoustic and electromagnetic timescales. The major contribution of the present work is the development of direct computation of wake vortex detection using RASS. Two methods that can make such a direct computation of a RASS feasible are proposed in this paper.

In the next section the basic equations for electromagnetic and acoustic wave propagation are presented. The Abel transform is also described. The Abel transform is applied to the output of the RASS simulation to retrieve the radial variation of the wake vortex velocity. The application of the Abel transform is not limited to the numerical calculation and could be used in practice to retrieve the wake vortex velocity field. The numerical implementation is then given including a description of the difficulties in obtaining a time-accurate

Received 29 April 2000; presented as Paper 2000-2073 at the AIAA/CEAS 6th Aeroacoustics Conference, Lahaina, HI, 12–14 June 2000; revision received 5 December 2000; accepted for publication 15 December 2000.

*Postdoctoral Research Associate, Department of Aerospace Engineering. Member AIAA.

†Boeing/A. D. Welliver Professor, Department of Aerospace Engineering. Associate Fellow AIAA.

simulation and methods to overcome these difficulties. This is followed by some example results and conclusions.

II. Analysis

A RASS is a device that uses scattering of electromagnetic waves in a nonhomogeneous medium enhanced by acoustic waves. Therefore, Maxwell's equations for media with nonuniform permittivity and the linearized Euler equations for media with nonuniform mean flow are the main framework for the RASS simulation. Furthermore, the relationship between the permittivity perturbation and density (or pressure) fluctuations has to be modeled. Each of these is discussed in the following sections.

A. Equations for Electromagnetic Wave Propagation and Scattering

The propagation and scattering of electromagnetic waves satisfy the Maxwell equations. The Maxwell equations for a nonconductive medium without charge can be written as

$$\nabla \times \boldsymbol{E} = -\frac{\partial \boldsymbol{B}}{\partial t} \tag{2}$$

$$\nabla \times \boldsymbol{H} = \frac{\partial \boldsymbol{D}}{\partial t} \tag{3}$$

$$\nabla \cdot \boldsymbol{D} = 0 \tag{4}$$

$$\nabla \cdot \boldsymbol{B} = 0 \tag{5}$$

where

$$\boldsymbol{D} = \epsilon \boldsymbol{E} \tag{6}$$

$$\boldsymbol{B} = \mu \boldsymbol{H} \tag{7}$$

and $\boldsymbol{E}$ is the electric field intensity vector (V/m), $\boldsymbol{H}$ the magnetic field intensity vector (A/m), $\boldsymbol{D}$ the electric displacement density (C/m^2), $\boldsymbol{B}$ the magnetic flux density (T), ϵ the permittivity (F/m), and μ the permeability (H/m).

Therefore

$$\nabla \times \boldsymbol{E} = -\frac{\partial(\mu \boldsymbol{H})}{\partial t} \tag{8}$$

$$\nabla \times \boldsymbol{H} = \frac{\partial(\epsilon \boldsymbol{E})}{\partial t} \tag{9}$$

These equations can be applied to the total field:

$$\boldsymbol{E}_t = \boldsymbol{E}_i + \boldsymbol{E}_s$$

$$\boldsymbol{H}_t = \boldsymbol{H}_i + \boldsymbol{H}_s$$

where the subscripts t, i, and s refer to total, incident, and scattered fields, respectively. Thus

$$\nabla \times \boldsymbol{E}_t = -\frac{\partial(\mu \boldsymbol{H}_t)}{\partial t} \tag{10}$$

$$\nabla \times \boldsymbol{H}_t = \frac{\partial(\epsilon \boldsymbol{E}_t)}{\partial t} \tag{11}$$

The incident field satisfies the free space equations:

$$\nabla \times \boldsymbol{E}_i = -\mu_0 \frac{\partial(\boldsymbol{H}_i)}{\partial t} \tag{12}$$

$$\nabla \times \boldsymbol{H}_i = \epsilon_0 \frac{\partial(\boldsymbol{E}_i)}{\partial t} \tag{13}$$

Subtracting the incident field [Eqs. (12) and (13)] from the total field [Eqs. (10) and (11)] yields

$$\nabla \times \boldsymbol{E}_s = -\frac{\partial}{\partial t}(\mu \boldsymbol{H}_s) - \frac{\partial}{\partial t}[(\mu - \mu_0)\boldsymbol{H}_i] \tag{14}$$

$$\nabla \times \boldsymbol{H}_s = \frac{\partial}{\partial t}(\epsilon \boldsymbol{E}_s) + \frac{\partial}{\partial t}[(\epsilon - \epsilon_0)\boldsymbol{E}_i] \tag{15}$$

These are the basic equations for the scattered field. To eliminate $\boldsymbol{H}_s$, take the curl of Eq. (14):

$$\nabla \times (\nabla \times \boldsymbol{E}_s) = -\frac{\partial}{\partial t}[(\nabla \times (\mu \boldsymbol{H}_s)] - \frac{\partial}{\partial t}\{\nabla \times [(\mu - \mu_0)\boldsymbol{H}_i]\} \tag{16}$$

It is assumed that μ is constant throughout the scattered field. In fact, experimental evidence shows that the permeability remains the same as for free space. Therefore, $\mu = \mu_0$. Then if $\nabla \times \boldsymbol{H}_s$ is substituted from Eq. (15);

$$\nabla(\nabla \cdot \boldsymbol{E}_s) - \nabla^2 \boldsymbol{E}_s = -\mu \frac{\partial^2}{\partial t^2}(\epsilon \boldsymbol{E}_s) - \mu \frac{\partial^2}{\partial t^2}[(\epsilon - \epsilon_0)\boldsymbol{E}_i] \tag{17}$$

where, in Eq. (17), the vector identity $\nabla \times (\nabla \times \boldsymbol{E}_s) = \nabla(\nabla \cdot \boldsymbol{E}_s) - \nabla^2 \boldsymbol{E}_s$ has been used.

The local change in density and temperature gives rise to a variation in the permittivity of the medium. So, the timescale of the electromagnetic (EM) field is much shorter than the timescale for a change in ϵ because the variation of permittivity is proportional to the acoustic frequency. Therefore

$$\nabla(\nabla \cdot \boldsymbol{E}_s) - \nabla^2 \boldsymbol{E}_s + \frac{1}{c^2}\frac{\partial^2 \boldsymbol{E}_s}{\partial t^2} = -\mu \frac{\partial^2}{\partial t^2}(\Delta \epsilon \boldsymbol{E}_i) \tag{18}$$

where $c = (\mu_0 \epsilon_0)^{-1/2}$ is the speed of light and $\Delta \epsilon = \epsilon - \epsilon_0$. Equation (18) neglects multiple scattering.

B. Equations for Acoustic Wave Propagation

The propagation and scattering of acoustic waves are described by the linearized Euler equations. The two-dimensional Euler equations in conservative form can be written as

$$\frac{\partial \boldsymbol{Q}}{\partial t} + \frac{\partial \boldsymbol{G}}{\partial x} + \frac{\partial \boldsymbol{F}}{\partial y} = \boldsymbol{S} \tag{19}$$

where

$$\boldsymbol{Q} = \begin{Bmatrix} \rho \\ \rho u \\ \rho v \\ \rho e_t \end{Bmatrix}, \qquad \boldsymbol{G} = \begin{Bmatrix} \rho u \\ \rho u^2 + p \\ \rho uv \\ (\rho e_t + p)u \end{Bmatrix}, \qquad \boldsymbol{F} = \begin{Bmatrix} \rho v \\ \rho uv \\ \rho v^2 + p \\ (\rho e_t + p)v \end{Bmatrix}$$

The variables ρ, p, and e_t are the density, pressure, and total energy, respectively. The total energy is defined by

$$e_t = c_v T + |\boldsymbol{u}|^2/2 \tag{20}$$

where c_v is the specific heat at constant volume; T is the temperature; $\boldsymbol{u}$ is the velocity vector; and t, u, and v represent time and the two Cartesian velocity components, respectively. In Eq. (19), $\boldsymbol{S}$ represents the acoustic source terms.

In linear acoustics all physical variables are decomposed into their mean parts and perturbation quantities. These perturbations are very small so that second-order products of these quantities may be ignored. By substitution of the physical variables into Eq. (19) and neglecting all second-order and higher-order terms of perturbation quantities, the linearized Euler equations can be obtained. In the RASS simulation the acoustic source is located far from the vortex center. Therefore, the mean flow velocity in the vicinity of the source is negligible. This makes it possible to ignore the effect of the source on the right-hand side of the momentum equations and also allows the replacement of the right-hand side of the energy equation by $c_{a0}^2 S$, where c_{a0} is the free space sound speed. The governing

differential equations for a two-dimensional flow with nonuniform mean flow quantities then become

$$\frac{\partial \rho'}{\partial t}+\rho'\left(\frac{\partial \bar{u}}{\partial x}+\frac{\partial \bar{v}}{\partial y}\right)+\bar{\rho}\left(\frac{\partial u'}{\partial x}+\frac{\partial v'}{\partial y}\right)+u'\frac{\partial \bar{\rho}}{\partial x}+v'\frac{\partial \bar{\rho}}{\partial y}+\bar{u}\frac{\partial \rho'}{\partial x}+\bar{v}\frac{\partial \rho'}{\partial y}=S$$

$$\frac{\partial u'}{\partial t}+\bar{u}\frac{\partial u'}{\partial x}+\bar{v}\frac{\partial u'}{\partial y}+u'\frac{\partial \bar{u}}{\partial x}+v'\frac{\partial \bar{u}}{\partial y}+\frac{\rho'}{\bar{\rho}}\left(\bar{u}\frac{\partial \bar{u}}{\partial x}+\bar{v}\frac{\partial \bar{u}}{\partial y}\right)+\frac{1}{\bar{\rho}}\frac{\partial p'}{\partial x}=0$$

$$\frac{\partial v'}{\partial t}+\bar{u}\frac{\partial v'}{\partial x}+\bar{v}\frac{\partial v'}{\partial y}+u'\frac{\partial \bar{v}}{\partial x}+v'\frac{\partial \bar{v}}{\partial y}+\frac{\rho'}{\bar{\rho}}\left(\bar{u}\frac{\partial \bar{v}}{\partial x}+\bar{v}\frac{\partial \bar{v}}{\partial y}\right)+\frac{1}{\bar{\rho}}\frac{\partial p'}{\partial y}=0$$

$$\frac{\partial p'}{\partial t}+\gamma p'\left(\frac{\partial \bar{u}}{\partial x}+\frac{\partial \bar{v}}{\partial y}\right)+\gamma \bar{p}\left(\frac{\partial u'}{\partial x}+\frac{\partial v'}{\partial y}\right)+u'\frac{\partial \bar{p}}{\partial x}+v'\frac{\partial \bar{p}}{\partial y}+\bar{u}\frac{\partial p'}{\partial x}+\bar{v}\frac{\partial p'}{\partial y}=c_{a0}^2 S \tag{21}$$

where an overbar indicates a mean quantity and primes denote fluctuations about the mean.

In the present study the form of the acoustic source $S(x, y, t)$ is taken to be

$$S(x, y, t)=\xi\Phi(t)\exp\left\{-\sigma_s\left[(x-x_0)^2+(y-y_0)^2\right]\right\}\sin\omega_a t \tag{22}$$

where

$$\Phi(t)=\exp\left[-\sigma_t(t-t_0)^2\right]$$

and t_0 is the pulse delay time; ξ, σ_s, and σ_t are parameters that control the amplitude and the width of the pulse in space and time, respectively. The acoustic frequency is ω_a and the source is located at (x_0, y_0).

C. Permittivity Variations in Atmosphere

According to Falcone,[4] the permittivity in the atmosphere can be written as

$$\epsilon=1+[(1.5514\times10^{-6}p)/T]\left\{1+[(4.8067\times10^{3})/T](p_{\mathrm{wv}}/p)\right\} \tag{23}$$

where T is the temperature in Kelvin, p the total pressure in pascals, and p_{wv} is the partial pressure of water vapor, also in pascals. For a dry atmosphere $p_{\mathrm{wv}}=0$, and this formula can be simplified to

$$\epsilon=1+(1.5514\times10^{-6}p)/T \tag{24}$$

Let $T=300$ K and $p=\bar{p}+p'$, where $\bar{p}$ and p' are mean and acoustic pressure, respectively. Also let ϵ_0 be the permittivity of free space, i.e., where $p'\equiv0$. Then

$$\Delta\epsilon=\epsilon-\epsilon_0=5.1715\times10^{-9}p' \tag{25}$$

where p' is in pascals.

For a nondry atmosphere p_{wv} can be approximated by[5]

$$p_{\mathrm{wv}}=461.4948T\rho_v \tag{26}$$

where ρ_v is the absolute humidity in kilograms/cubic meters. In turn, ρ_v can be approximated by

$$\rho_v=(RH/100)\times10^{-3}b\exp\left(c_0+c_1b+c_2b^2\right),\qquad b=(273.15/T) \tag{27}$$

where RH is the relative humidity and

$$c_0=18.9766,\qquad c_1=-14.9595,\qquad c_2=-2.4388$$

Equations (23–27) make it possible to determine the permittivity perturbation $\Delta\epsilon$ caused by pressure fluctuations with the effects of mean temperature and humidity taken into account.

D. Vortex Models

The main objective of this paper is to reconstruct the velocity profile of any prespecified vortex through an analysis of the electromagnetic backscatterer. To demonstrate that the RASS can distinguish between different wake vortex velocity profiles, both Taylor and Oseen vortices are considered as two typical cases. As noted by de Neufville,[6] the vorticity distribution of any incompressible unsteady vortex may be written in terms of a linear combination of various vortex modes. Oseen and Taylor vortices correspond to the two leading modes in the general solution.

The Taylor vortex has the following tangential velocity profile[7]:

$$v_\theta=(H/8\pi)(r/\nu t^2)\exp(-r^2/4\nu t) \tag{28}$$

The constant H is a measure of the vortex strength; t, ν, and r are time, the kinematic viscosity, and the radial distance, respectively. It is more convenient to write Eq. (28) in terms of core radius r_c and core velocity V_c:

$$v_\theta/V_c=(r/r_c)\exp\left\{\tfrac{1}{2}\left[1-(r/r_c)^2\right]\right\} \tag{29}$$

The circulation of the Taylor vortex approaches zero when it is calculated on a contour with large radius, and so it is not very representative of an aircraft wake vortex. As just noted, it is used here simply to demonstrate the capability of the RASS to determine different tangential velocity profiles.

An Oseen vortex is described by[8]

$$v_\theta=(\Gamma/2\pi r)[1-\exp(-r^2/4\nu t)] \tag{30}$$

where Γ is a constant and represents the total circulation of the vortex. In terms of core radius and velocity, an Oseen vortex can be described by

$$v_\theta/V_c=\alpha(r_c/r)\left\{1-\exp\left[-\beta(r/r_c)^2\right]\right\} \tag{31}$$

where $\alpha=1.397950$ and $\beta=1.256435$ are chosen such that the maximum velocity occurs at the core radius.

E. Abel Transform

The analysis of the EM scattered signal can only reveal the component of the wake vortex velocity profile in the direction of the incident radar beam. However, one can use this velocity information and still retrieve the vortex velocity field. The problem of determining a function $f(x, y)$ from knowledge of its line integrals, in the two-dimensional case, or a function $f(x, y, z)$ from integrals over planes, in the three-dimensional case, arises in widely diverse fields. The Abel transform and its inverse form the mathematical framework common to this class of problems.

The Abel transform and its inverse can be expressed in terms of the following integral relations[9]:

$$Q(x)=\int_x^R\frac{g(r)\,\mathrm{d}r}{\sqrt{r^2-x^2}} \tag{32}$$

$$g(r)=-\frac{2}{\pi}\frac{\mathrm{d}}{\mathrm{d}r}\int_r^R\frac{xQ(x)\,\mathrm{d}x}{\sqrt{x^2-r^2}}$$

$$0\le x\le r\le R\le+\infty \tag{33}$$

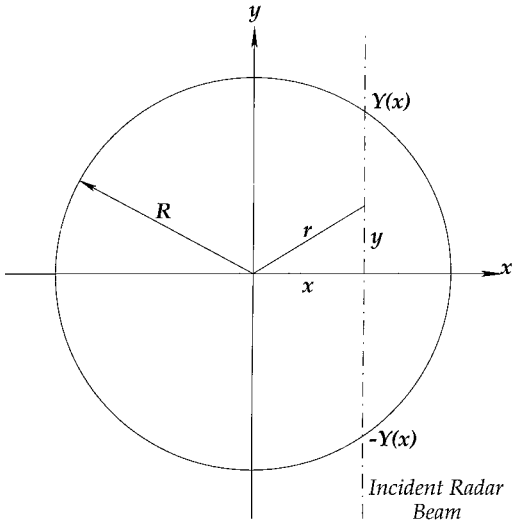

Fig. 1 Application of the Abel transform to wake vortex velocity.

Equation (33) may be written as

$$g(r) = \frac{2r}{\pi}\left[\frac{Q(R)}{\sqrt{R^2 - r^2}} - \int_r^R \frac{Q'(x)\,\mathrm{d}x}{\sqrt{x^2 - r^2}}\right] \tag{34}$$

where $Q'(x)$ represents the derivative of $Q(x)$ with respect to x.

Now consider an axisymmetric vortex velocity field $V(r)$ in the domain shown in Fig. 1. In the RASS measurements the Doppler shift of the EM scattered field is not proportional to the wake vortex velocity, but to the wake vortex velocity component in the transmitter direction, i.e., $V(r)x/r$, where r is the radial distance and x is the radar beam location as shown in Fig. 1. Therefore,

$$Q(x) = \int_{-Y(x)}^{Y(x)} \frac{x}{r} V(r)\,\mathrm{d}y, \qquad 0 \le x \le R \tag{35}$$

may be obtained for any given radar beam location x once the backscattered echo is analyzed. This integral can also be written in terms of the variable r for any given x:

$$\frac{Q(x)}{x} = 2\int_{r=x}^{R} \frac{V(r)\,\mathrm{d}r}{\sqrt{r^2 - x^2}} \tag{36}$$

Then from Eq. (33)

$$V(r) = -\frac{1}{\pi}\frac{\mathrm{d}}{\mathrm{d}r}\int_r^R \frac{Q(x)\,\mathrm{d}x}{\sqrt{x^2 - r^2}} \tag{37}$$

or equivalently from Eq. (34)

$$V(r) = \frac{1}{\pi r}\left[\frac{RQ(R)}{\sqrt{R^2 - r^2}} - \int_r^R \frac{xQ'(x)\,\mathrm{d}x}{\sqrt{x^2 - r^2}}\right] \tag{38}$$

If $Q(x)$ is known as a closed-form function, integrals (37) or (38) can be evaluated, at least formally, to determine $V(r)$. In practice, however, $Q(x)$ is available as a discrete data set, and a numerical technique has to be used. Here, the numerical method proposed by Nestor and Olsen[10] has been applied. This method has been slightly modified to best fit the RASS application.

III. Numerical Implementation

The scattering problem is divided into two parts, namely acoustic and electromagnetic scattering. In the first the acoustic scattered field is determined numerically. The linearized Euler equations are discretized using a fourth-order dispersion-relation-preserving (DRP) algorithm[11] in space and a fourth-order Runge–Kutta scheme in time.

The interaction between the acoustic and electromagnetic waves comes from the fact that the pressure fluctuations caused by the propagation of the acoustic waves can perturb the permittivity in the Maxwell's equations. In fact, the pressure fluctuations act as a forcing function for the scattered EM field, as is clear from Eq. (18). Once the acoustic field is reconstructed at any instant, the permittivity perturbation $\Delta\epsilon$ and, therefore, the right-hand side of Eq. (18) or Eq. (48) is determined. Then, the electromagnetic scattering problem is solved using a second-order central difference scheme both in space and time. No artificial dissipation is used in the Maxwell solver. The incident field is specified from an analytical solution. Because the speeds of sound and light are so different, the medium, including the vortex and acoustic field, appear frozen in time relative to the electromagnetic wave. Thus, the electromagnetic wave is assumed to be propagating through a stationary, nonuniform medium. In fact, few hundred iterations in the Maxwell solver take place between each time step of the Euler calculation.

In both cases of acoustic and electromagnetic scattering, a radiation boundary condition is used. For the Euler calculation the radiation boundary condition developed by Tam and Webb[11] is used. For the Maxwell calculation the nonreflecting boundary condition described by Bayliss and Turkell[12] is applied.

The numerical schemes that are used in this paper are well-established schemes, and their various numerical aspects have been examined in many publications including Tam and Webb's original paper on the DRP scheme[11]; therefore, they are not repeated here. A comparison between a numerical solution of the RASS model problem and its analytical solution has been given by Boluriaan,[13] which shows a nearly perfectly agreement for the model problem considered.

A. Computational Requirements for a Time-Accurate RASS Simulation

The resolution of the discrete Fourier transform can be written as $1/NT$ Hz, where N is the number of samples and $1/T$ is the sampling rate in hertz. For the one-dimensional RASS simulation

$$\Delta x = \lambda_e / M \tag{39}$$

where M is the number of grid points per wavelength. Because the Courant–Friedrichs–Lewy (CFL) number, denoted by σ, is equal to $c\Delta t/\Delta x$, then

$$\Delta t = \sigma\lambda_e / cM \tag{40}$$

or

$$\text{sampling rate} = cM/\sigma\lambda_e \tag{41}$$

Because $c\lambda_e = f_e$, we obtain

$$\text{resolution} = Mf_e/\sigma N \tag{42}$$

According to Nalbandyan,[14] the Doppler shift caused by a change of the local sound speed is

$$\omega_d = 2k_e U \tag{43}$$

which may also be written as

$$f_d = (2f_e/c)U \tag{44}$$

where f_d and f_e are the Doppler shifted frequency and radar wave frequency, respectively, both in hertz, and U is the local vortex velocity component in the transmitter direction. A resolution at least equal to the Doppler shift is required. Thus,

$$(2f_e/c)U \ge Mf_e/\sigma N \tag{45}$$

or

$$N \ge Mc/2U\sigma \tag{46}$$

The number of grid points per wavelength M is usually taken to be 10–15. Therefore, in order to detect a vortex wake velocity with a resolution of 0.1 m/s requires that

$$N \ge \frac{10 \times 3 \times 10^8}{2 \times 0.1} = 1.5 \times 10^{10} \qquad \text{samples}$$

This assumes that $\sigma = 1$.

This number of samples is not feasible, simply because it would take several months of CPU time to collect 1.5×10^{10} samples even on the fastest available multiprocessor computers. Recall that there

is a finite computational time required to obtain each time sample. Furthermore, usually a resolution of at least 10–50 times the Doppler shift is desired.

A possible way to overcome this difficulty is to notice that the number of required samples given by Eq. (46) is linearly proportional to the speed of light. Therefore, if a fictitious speed of light (e.g., 3×10^5 m/s instead of 3×10^8 m/s) is used in the simulation, it is possible to apply an explicit scheme and obtain time-accurate results in a reasonable CPU time. In the "Results" section it will be shown that all of the essential characteristics of the received scattered field can be captured using such a fictitious speed of light.

B. Equations for the Demodulated Scattered Field

Another way to make the RASS simulation computationally feasible is to try to remove the incident electromagnetic frequency and recast the governing equation (18) in terms of the modulation of the carrier frequency. To do so, one can write

$$\boldsymbol{E}_s = \hat{\boldsymbol{E}}_s e^{i\omega_e t} \tag{47}$$

where ω_e is the frequency of the incident electromagnetic waves and $\hat{\boldsymbol{E}}_s$ is the scattered electromagnetic field after removal of the carrier frequency. Substitution of Eq. (47) into Eq. (18) yields

$$\nabla(\nabla \cdot \hat{\boldsymbol{E}}_s) - \nabla^2 \hat{\boldsymbol{E}}_s + \frac{1}{c^2}\frac{\partial^2 \hat{\boldsymbol{E}}_s}{\partial t^2} + \frac{2i\omega_e}{c^2}\frac{\partial \hat{\boldsymbol{E}}_s}{\partial t} - \frac{\omega_e^2}{c^2}\hat{\boldsymbol{E}}_s = -\mu e^{-i\omega_e t}\frac{\partial^2}{\partial t^2}(\Delta \epsilon \boldsymbol{E}_i) \tag{48}$$

The frequency content of $\hat{\boldsymbol{E}}_s$ is of the order of the acoustic frequency, which is significantly lower than the incident electromagnetic frequency. Therefore, a substantially lower sampling rate is required to reveal this frequency according to the Nyquist criterion. A lower sampling rate means a higher time step, which leads to a higher CFL number. The maximum allowable CFL number is restricted by the stability criterion for explicit schemes. Implicit scheme may be used to overcome this difficulty. A higher CFL number also improves the resolution of the fast Fourier transform substantially according to Eq. (42) for a given number of samples.

A simple von Neumann stability analysis shows that for an explicit second-order central difference approximation the one-dimensional Maxwell solver is stable if CFL ≤ 1. Because the speed of light is constant, CFL $= 1$ gives a nondispersive, nondissipative scheme independent of phase angle.

More interesting results are obtained from a consideration of the governing equation after demodulation. In this case the governing equation is a partial differential equation with complex coefficients. Figures 2 and 3 show the results of a stability analysis of the discretized form of Eq. (48). For this analysis an implicit second-order central difference approximation in both time and space is used. Figure 2 shows the maximum absolute value of the eigenvalues as a function of CFL number. It can be seen from the figure that the modes associated with λ_2 are stable as Max$|\lambda_2|$ is less than 1 for all CFL numbers. In fact, Max$|\lambda_2|$ monotonically decreases as the CFL number increases. On the other hand, the modes associated with λ_1 are unstable up to CFL number about 1000, and then become stable.

In Fig. 3 the absolute value of the eigenvalues of the amplification matrix have been plotted as a function of the phase angle for different CFL numbers. It can be seen from the figure that the scheme is highly dissipative for large CFL numbers. A similar calculation shows that the scheme is also dispersive for large CFL numbers. This means that for high CFL numbers the results will not be time accurate. A highly dispersive scheme will change the phase angle, wave form, and wave speed of the solution. However, the frequency of the wave remains the same if the governing differential equations are linear. Therefore, the solution is frequency accurate, the only factor that matters for the RASS application. An elegant aspect of RASS lies in the fact that

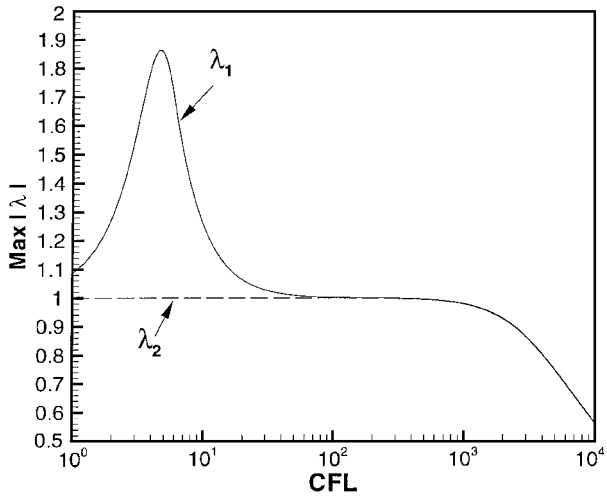

Fig. 2 Effect of CFL number on the maximum value of the amplification factor.

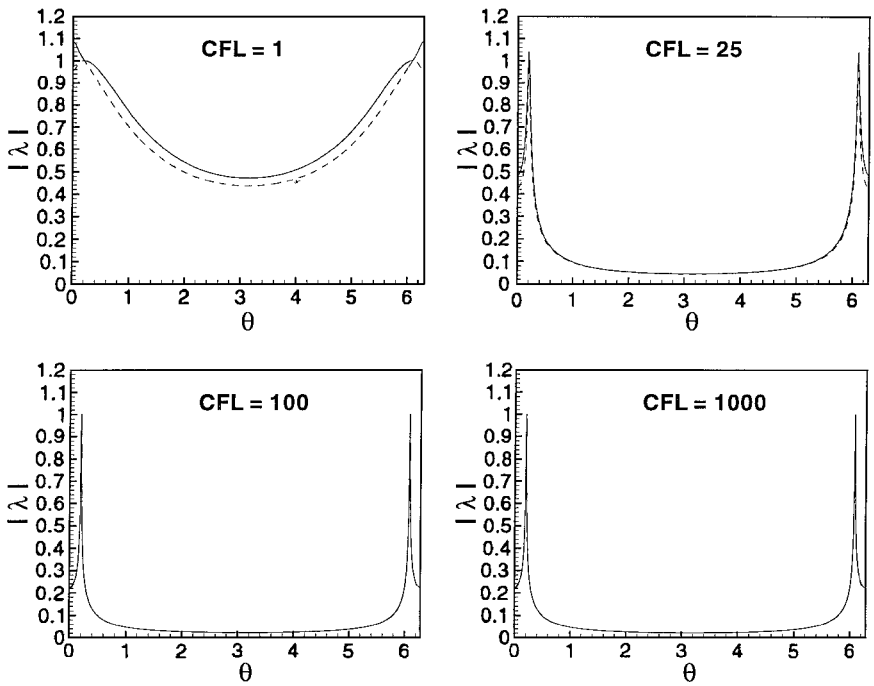

Fig. 3 Effect of CFL number on amplification factor: ——, $|\lambda_1|$; and – – –, $|\lambda_2|$.

the wake vortex velocity information is embedded in the Doppler shift, and not in the amplitude or phase of the backscattered signal.

IV. Results

A. Parallel Performances

The code is written in Fortran 90 with the message passing interface as the parallel implementation. It is portable to several platforms, and it has been tested successfully on an IBM SP2, an SGI Power Challenge, and a PC Cluster running under a Linux operating system. A two-dimensional domain decomposition is used.

The Euler solver calculates the pressure perturbation at each grid point. These pressure perturbations have to be transferred to the Maxwell solver in order to determine the permittivity fluctuations at each grid point and at each time step. This could be very costly, if it requires processor-to-processor communications. To avoid this, the Maxwell and Euler solvers share the same grid points on each processor. The message passing is then only performed along the processors' boundaries, which minimizes the communication time, and therefore makes the code more scalable.

The scalability of the code has been examined on two different platforms. Figure 4 shows the scalability results. As is clear from the figure, the code is nearly perfectly scalable on both platforms for the number of processors considered.

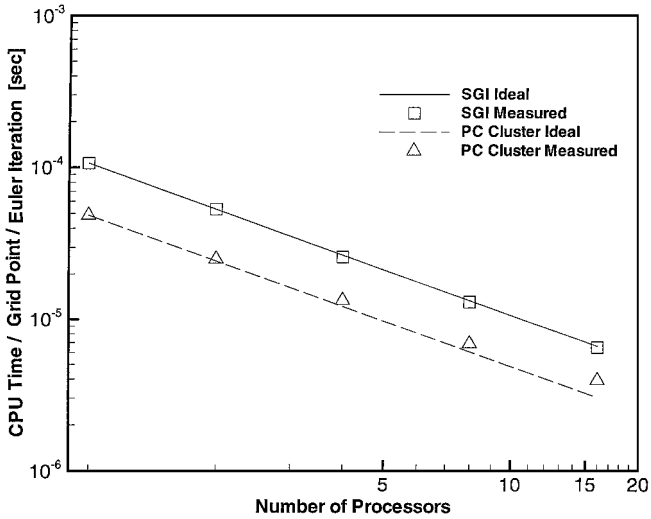

Fig. 4 Parallel performance on different computer platforms.

B. Effect of Bragg Condition

Figure 5 shows the effect of the Bragg condition on the scattered field. In these results the mean flow velocity is zero, and a continuous incident electromagnetic wave has been used. As one can see from the figure, even a very small deviation from the Bragg condition leads to a significant effect on the scattered field. Figure 5 also shows that for a one-dimensional Maxwell simulation forward scattering is negligible compared to backscattering.

C. Model Problem for Uniform Mean Flow

A uniform mean flow is used to validate the code. For uniform mean flow the Euler equations can be solved analytically, and only the Maxwell equations need to be solved numerically. A continuous electromagnetic incident field and an acoustic pulse, approximately equal to three acoustic wavelengths, are considered. The mean flow velocity is chosen to be 50 m/s. The code is run for implicit and explicit cases.

In the explicit case a fictitious speed of light equal to 3×10^5 m/s and an electromagnetic incident frequency equal to 900 kHz are considered. The incident acoustic frequency is chosen appropriately to meet the Bragg condition. The power spectrum of the simulated scattered signal is shown in Fig. 6. The frequency resolution in this plot is 21.572 Hz, which corresponds to 3.595 m/s. This is the minimum frequency difference (or velocity difference) that can be resolved from this spectrum. The power spectrum resolution can be improved further using zero padding. The tradeoff is the spurious side lobes that grow as the number of added zeros increases. The Doppler shift given by the spectrum in Fig. 6 equals 2340.8 Hz, of which 2040 Hz is caused by the local sound speed and 300.8 is caused by the vortex velocity contribution. The frequency shift of 300.8 Hz corresponds to 50.133 m/s for the given conditions. The difference between the velocity that calculated from the Doppler shift and the exact value of the mean flow velocity is within the resolution of the Fourier transform. The power spectrum level in Fig. 6 is arbitrary.

Figure 7 shows the power spectrum of the scattered signal obtained from a solution of the demodulated equation. The incident electromagnetic frequency in this case is taken to be 900 MHz, and the governing differential equation is solved using an implicit scheme with a large time step. The incident acoustic frequency equals 2040 Hz in order to satisfy the Bragg condition. The incident acoustic frequency is also shown in the figure. The resolution in this plot is the same as in Fig. 6. The Doppler shift in the spectrum corresponds to a mean flow velocity equal to 51.884 m/s. The accuracy of this measured velocity is also within the Fourier transform

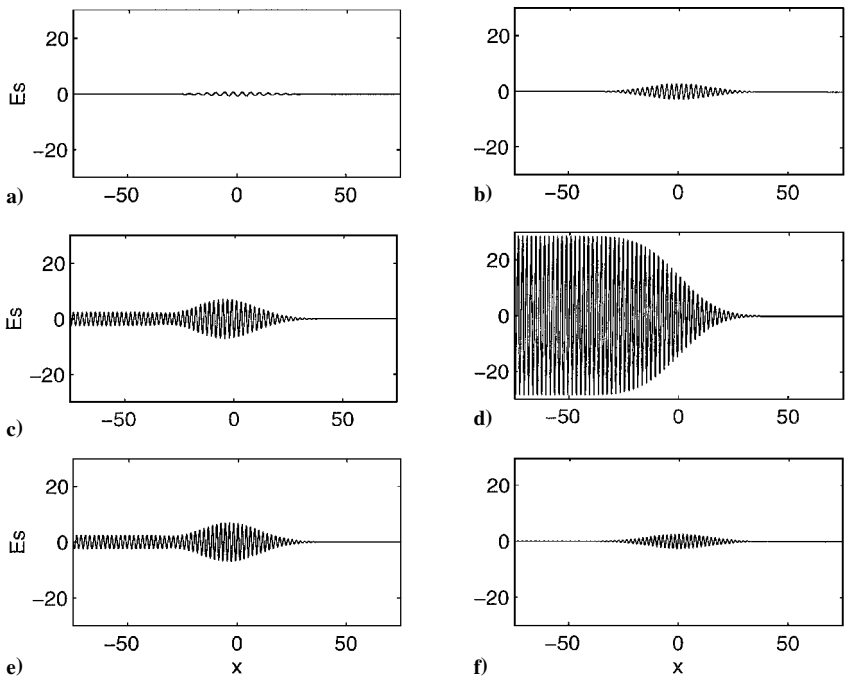

Fig. 5 Effect of Bragg condition on the scattered field: a) $\lambda_e/\lambda_a = 1.5$, b) $\lambda_e/\lambda_a = 1.9$, c) $\lambda_e/\lambda_a = 1.95$, d) $\lambda_e/\lambda_a = 2.0$, e) $\lambda_e/\lambda_a = 2.05$, and f) $\lambda_e/\lambda_a = 2.1$.

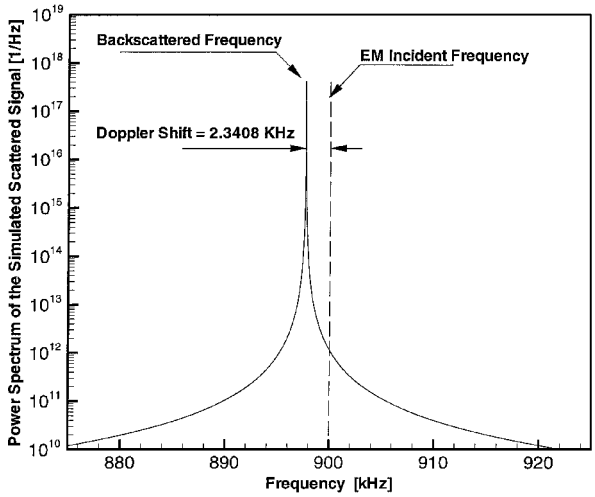

Fig. 6 Power spectrum of the simulated scattered signal in uniform mean flow.

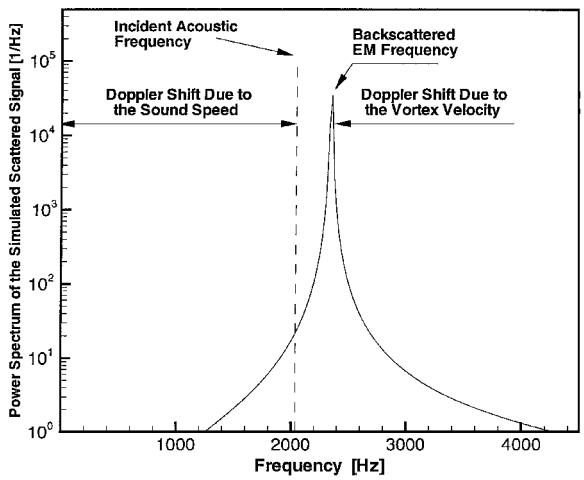

Fig. 7 Power spectrum of the simulated scattered signal in uniform mean flow after removal of the carrier frequency.

resolution. Although in this case a large CFL number and a highly dissipative scheme is used, the mean flow velocity is obtained with the same accuracy as the explicit scheme.

D. Combined Euler and Maxwell Simulation Results

Figure 8 shows the computational domain for the direct computation of a RASS. The vortex core radius is chosen to be $10\lambda_a$, which is a typical size for aircraft wake vortices. An acoustic source is located at a distance equal to $38\lambda_a$ from the vortex center. The scattered electromagnetic signal is sampled $1.5\lambda_a$ above the source. The layout represents a monostatic RASS configuration with a very narrow beam radar transmitter.

For the implicit scheme the code is run for the typical operating values that are used in practice. The incident electromagnetic frequency is taken to be 900 MHz. This gives an acoustic wavelength, to meet the Bragg condition, of 0.167 m, which corresponds to an acoustic frequency of 2040 Hz.

The code is run for different positions of the incident radar beam, from within to the outside the vortex core. Figure 9 shows a typical backscattered electromagnetic signal for a Taylor vortex. In this particular figure the incident EM beam is $12.5\lambda_a$ away from the vortex center in the x direction. This time series data carry vortex velocity information in the direction of the incident radar beam. To extract this information, the signal is divided into a number of slices, and the power spectrum of each slice is calculated. The Doppler shift associated with the power spectrum of each slice gives the vortex velocity that corresponds to the location from which this particular slice came (for example, point Y in Fig. 8). It is then necessary to relate the signal arrival time to the position Y:

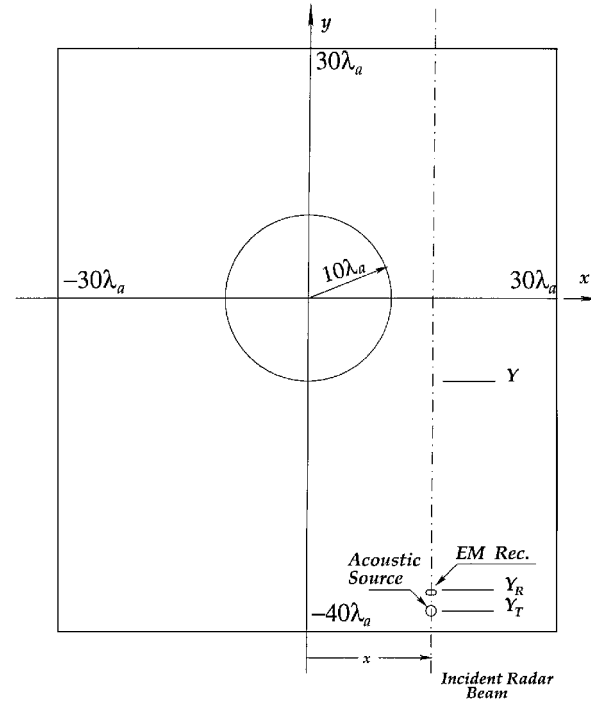

Fig. 8 Computational domain.

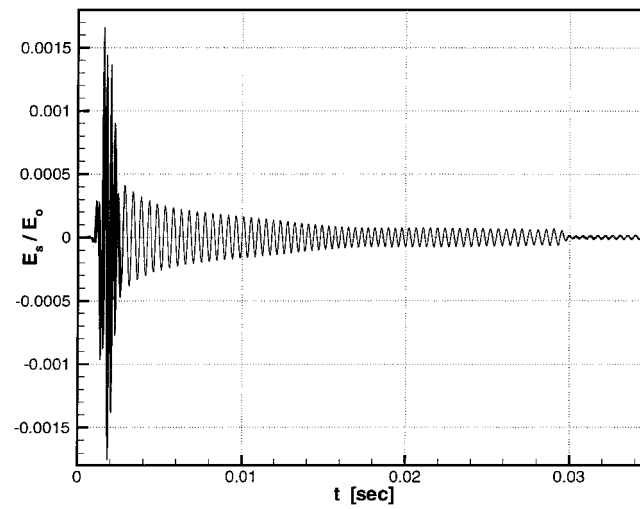

Fig. 9 Backscattered EM signal from Taylor vortex. The incident EM beam is $12.5\lambda_a$ away from the vortex center in the x direction.

$$\text{arrival time} = t_0 + t_{\text{AC}} + t_{\text{EM}}$$

where t_0 is the pulse delay time, t_{AC} the time required for the acoustic pulse to reach to the position Y, and t_{EM} the time required for the EM scattered signal to return to the receiver from position Y.

The pulse delay time is a prespecified value in the code and is known. t_{EM} can be easily calculated because the electromagnetic wave speed is constant within the solution domain:

$$t_{\text{EM}} = [(Y - Y_R)/c] \tag{49}$$

t_{AC} depends on the local sound speed and local vortex velocity, and the latter is unknown beforehand. To overcome this difficulty, t_{AC} is determined first assuming no mean flow, and then, based on the calculated vortex velocity, t_{AC} is adjusted. This process could be repeated any number of times. However, the numerical experiments show that the adjustments after the first correction are very small.

Figure 10 shows the vortex velocity profile for the data set of Fig. 9. In this figure the vertical axis represents the vortex velocity component in the transmitter direction. This velocity is normalized by the vortex core velocity. The solid line shows the exact velocity profile. The triangles and circles represent the vortex velocity before

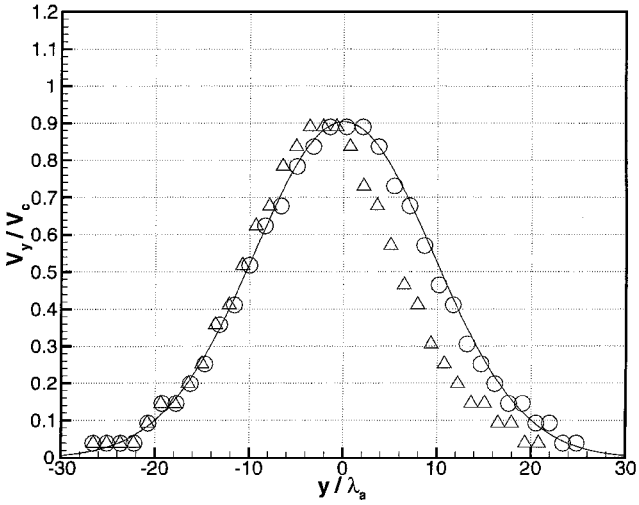

Fig. 10 The *y* component of the wake vortex velocity profile for a Taylor vortex. The incident EM beam is $12.5\lambda_a$ away from the vortex center in the *x* direction: ——, exact; △, first RASS simulation; and ○, corrected RASS simulation.

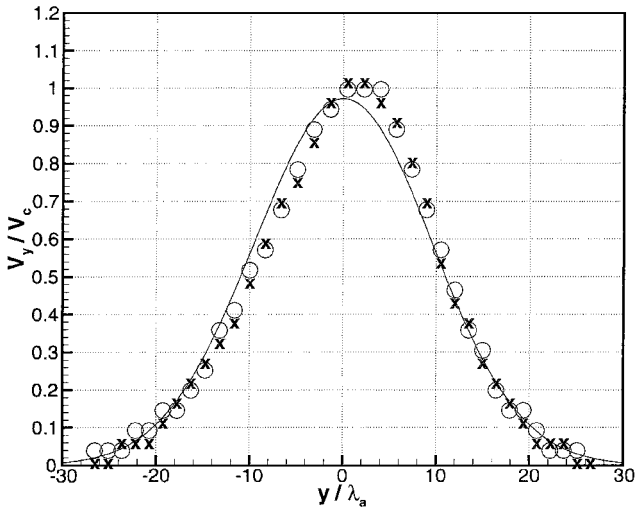

Fig. 11 The *y* component of the wake vortex velocity profile for a Taylor vortex. The incident EM beam is $8\lambda_a$ away from the vortex center in the *x* direction: ——, exact; ○, implicit; and ×, explicit.

and after the adjustment of t_{AC}, respectively. In this particular plot each slice of the time series consists of 40,000 samples, which corresponds to 0.0028 s. For the given operating condition this period of time covers a distance between 0.952–1.166 m depending upon the mean flow. In other words, each circle in Fig 10 shows the vortex velocity averaged over a distance roughly equal to 1 m.

In the explicit case with a fictitious speed of light, the speed of the electromagnetic wave is chosen to be 3×10^5 m/s. The incident EM frequency is reduced to 900 kHz to keep the EM wavelength the same as in the implicit case. The acoustic frequency and wavelength remain unchanged. Then the Bragg condition is met.

Figures 11–14 show the vortex velocity component in the transmitter direction along different radar beam locations and for both Taylor and Oseen vortices. In each plot the solid line shows the exact velocity profile. The results of the explicit and implicit RASS simulations are also shown. It can be seen that both schemes follow the exact profile with very good accuracy. The error associated with these results are within the resolution of the Fourier transform.

E. Application of the Abel Transform

In this section the Abel transform is applied to the results of both explicit and implicit schemes in order to retrieve the radial profile of the wake vortex tangential velocity. First, the velocity profile along the different locations of the incident radar beam is determined. In practice, this could be interpreted as a change in the relative vortex

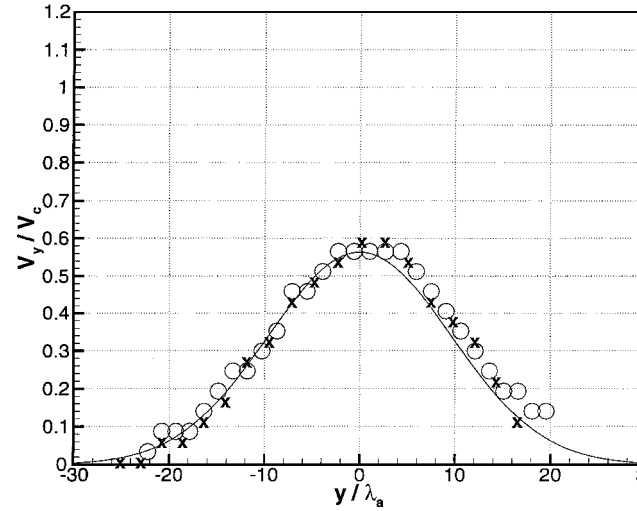

Fig. 12 The *y* component of the wake vortex velocity profile for a Taylor vortex. The incident EM beam is $20\lambda_a$ away from the vortex center in the *x* direction: ——, exact; ○, implicit; and ×, explicit.

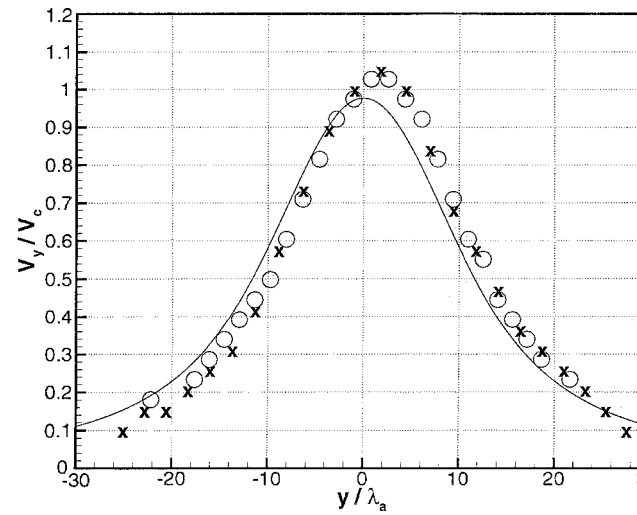

Fig. 13 The *y* component of the wake vortex velocity profile for an Oseen vortex. The incident EM beam is $8\lambda_a$ away from the vortex center in the *x* direction: ——, exact; ○, implicit; and ×, explicit.

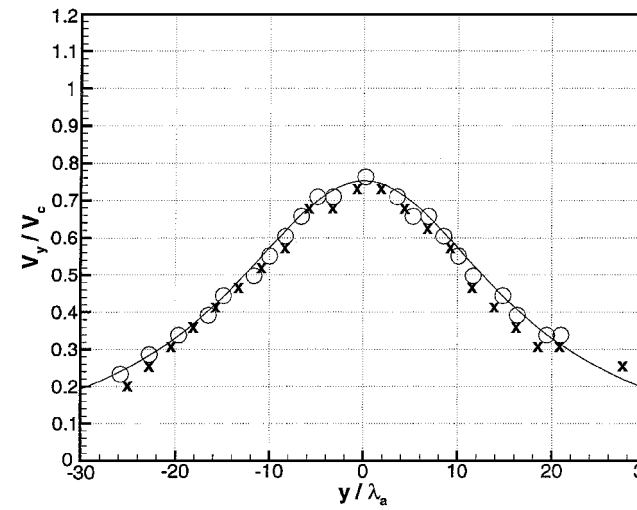

Fig. 14 The *y* component of the wake vortex velocity profile for an Oseen vortex. The incident EM beam is $20\lambda_a$ away from the vortex center in the *x* direction: ——, exact; ○, implicit; and ×, explicit.

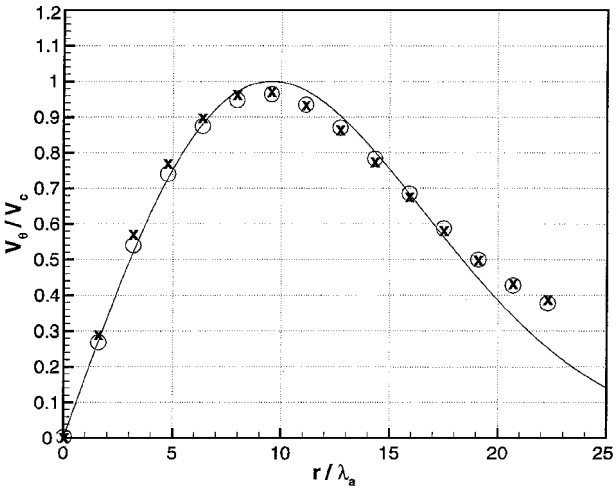

Fig. 15 Radial variation of the wake vortex tangential velocity for a Taylor vortex: ——, exact; ○, implicit; and ×, explicit.

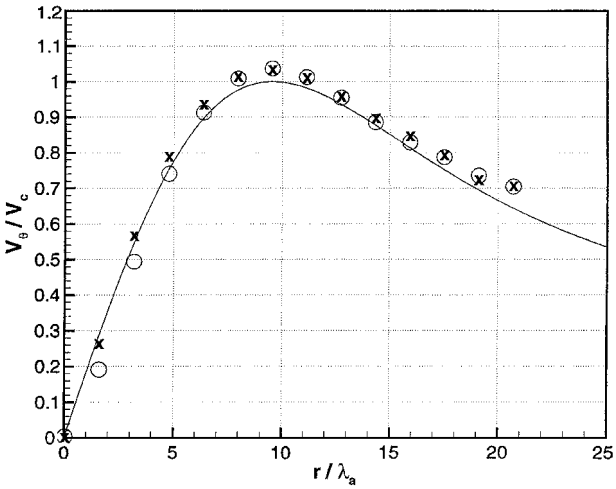

Fig. 16 Radial variation of the wake vortex tangential velocity for an Oseen vortex: ——, exact; ○, implicit; and ×, explicit.

location caused by convection of the wake vortex. The results are a series of plots similar to Figs. 11–14. Then $Q(x)$ is calculated from Eq. (35). In fact, $Q(x)$ is nothing but the area under the vortex velocity profile curve along any given radar beam location. Finally, $Q(x)$ is substituted into Eq. (38), and the radial wake vortex velocity distribution $V(r)$ is determined.

Figures 15 and 16 show the results of the Abel transform application for Taylor and Oseen vortices, respectively. As is clear from these figures, both implicit and explicit schemes reconstruct the vortex velocity profile with very good accuracy.

V. Conclusions

In this paper numerical simulations have been used to demonstrate that a RASS can determine the tangential velocity profile in a wake vortex as well as its location relative to the RASS transmitter and receiver. This has been achieved by analyzing the spectrum of the scattered electromagnetic signal in short time slices. These spectra provide the Doppler shift in the spectrum that determines the component of the vortex tangential velocity in the direction of the transmitter and the distance of that velocity value from the transmitter/receiver location.

To obtain results from the numerical simulations in a realistic computational time, two different approaches have been used. In the first the actual electromagnetic wave propagation speed has been replaced with a much lower value. This allows an explicit, time-accurate numerical scheme to be used. In the second a solution is obtained for the demodulated scattered signal. An implicit numerical method can then be used, and very large time steps can be taken. The latter method does not provide a time-accurate solution because of the highly dissipative nature of the numerical scheme, but it does contain the frequency information necessary to determine the vortex velocity and location. Neither of these approximations would be required in a real-time application of the technique where the scattered signal is the result of a physical process rather than a numerical simulation. However, the present results provide the framework for the real-time signal analysis.

A number of other simplifications have been made, in addition to those just described that are related to numerical issues. For simplicity, the vortex axis has been assumed to be normal to the direction of the RASS transmitter/receiver. This enables a two-dimensional simulation to be performed to describe the acoustic propagation problem. This will likely not be the case in reality where the vortex core may wander. However, suitable placement of the RASS relative to the glide path can make this inaccuracy less of an issue. In addition, the present electromagnetic simulation is one-dimensional and uses the permittivity results from the acoustic simulation along single lines. This is equivalent to assuming that the RASS transmitter and receiver have very narrow beams. In reality there will be a finite width to the transmitter beam and a finite capture angle for the antenna. The effect of these finite beam widths is the subject of ongoing study, but it is unlikely to change the principal conclusions of the present work.

The use of RASS for wake vortex detection offers considerable promise for practical incorporation into an aircraft vortex spacing system. It is an all weather device and relatively inexpensive compared to laser-based systems. In this paper we have provided a detailed simulation of the manner in which a RASS operates and have shown how it can provide quantitative descriptions of the vortex strength and location.

Acknowledgments

This study was supported in part by NASA Langley Research Center under Grant number NAG 1-1875. The Technical Monitor was Robert Neece.

References

[1] "Application of FAA Wake Vortex Research to Safety," U. S. Government Printing Office, No. 157, Washington, DC, July 1994.

[2] Doviak, R. J., and Zrnic, D. S., *Doppler Radar and Weather Observations*, 2nd ed. Academic Press, 1993, pp. 424–505.

[3] Rubin, W. L., Burnham, D. C., Spitzer, E. A., and Rudis, R. P., "A Robust Low Cost Airport Wake Vortex Sensor," AIAA Paper 2000-0627, Jan. 2000.

[4] Falcone, V. J., "Electromagnetic Wave Propagation in the Lower Atmosphere," *Handbook of Geophysics and Space Environment*, edited by A. S. Jursa, U.S. Air Force Geophysics Lab., 1985, Chap. 19.

[5] Grantham, D. D., Gringorten, I. I., and Kantor, A. J., "Water Vapor, Precipitation, Clouds, and Fog," *Handbook of Geophysics and Space Environment*, edited by A. S. Jursa, U.S. Air Force Geophysics Lab., 1985, Chap. 16.

[6] de Neufville, A. D., "The Dying Vortex," *Proceedings of the Fifth Midwestern Conference on Fluid Mechanics*, Univ. of Michigan, 1957, p. 365.

[7] Taylor, G. I., "On the Dissipation of Eddies," *The Scientific Papers of Sir Geoffrey Ingram Taylor*, Vol. 2, edited by G. K. Batchelor, Cambridge Univ. Press, Cambridge, England, U.K., 1960, pp. 96–101.

[8] Panton, R. L., *Incompressible Flow*, Wiley, New York, 1984, pp. 283–288.

[9] Gorenflo, R., and Vessella, S., "Abel Integral Equations, Analysis and Applications," *Lecture Notes in Mathematics*, Springer-Verlag, Berlin, 1991, pp. 35–37.

[10] Nestor, O. H., and Olsen, H. N., "Numerical Methods for Reducing Line and Surface Probe Data," *SIAM Review*, Vol. 2, No. 3, 1960, pp. 200–207.

[11] Tam, C. K. W., and Webb, J. C., "Dispersion-Relation-Preserving Finite Difference Schemes for Computational Aeroacoustics," *Journal of Computational Physics*, Vol. 107, No. 2, 1993, pp. 262–281.

[12] Bayliss, A., and Turkel, E., "Far Field Boundary Conditions for Compressible Flow," *Journal of Computational Physics*, Vol. 48, No. 2, 1982, pp. 182–199.

[13] Boluriaan, S., "Parallel Direct Numerical Simulation of Wake Vortex Detection Using Monostatic and Bistatic Radio Acoustic Sounding Systems," Ph.D. Dissertation, Dept. of Aerospace Engineering, Pennsylvania State Univ., Aug. 2000.

[14] Nalbandyan, O. G., "The Signal Frequency Spectrum in Radio Acoustic Sounding of the Atmosphere," *Izvestiya Atmospheric and Oceanic Physics*, Vol. 12, No. 7, 1976, pp. 772–774.

P. Givi
Associate Editor